

ANALYSIS OF THE INFLUENCE OF THE COMPOSITION OF THE SHIELDING GAS ON PRESSURE FORCE AND HEAT FLUXES IN ARC WELDING

Isabelle Choquet¹, Håkan Nilsson²

¹University West, Dept. of Engineering Science, Trollhättan, Sweden,

²Chalmers University of Technology, Dept. of Applied Mechanics, Gothenburg, Sweden

isabelle.choquet@hv.se

Abstract: A main problem raised by arc welding manufacturing is the determination of the optimal process parameters to ensure weld quality as well as resource efficient and sustainable production. To address this problem a better process understanding is required. In this study thermal magneto hydrodynamic modeling of a welding arc is used to reach a deeper insight into the influence of the composition of the shielding gas on the pressure force and the heat fluxes to a workpiece. The model was implemented in the open source simulation software OpenFOAM. Four different shielding gas mixtures combining argon and carbon dioxide were studied. When increasing the fraction of carbon dioxide the results show a significant increase of the arc velocity and temperature with constriction of the temperature field, a decrease of the pressure force and a significant increase of the heat fluxes on the base metal.

Keywords: thermal plasma, arc welding, shielding gas, arc pressure, heat flux, numerical simulation, OpenFOAM.

1. INTRODUCTION

Although used in manufacturing since many decades arc welding is still under intensive development to further improve weld quality, process productivity, and process control. Such improvements are also beneficial to both resource efficient and sustainable production. Electric arcs used in welding are generally coupling an electric discharge with a shielding gas to form a thermal shielding gas flow (i.e. a thermal plasma flow) with a temperature large enough to melt the materials to be welded. Gas Tungsten Arc (GTA) and Gas Metal Arc are the shielding arc welding processes the most used in production. The former in terms of amount of shielding gas consumed and the latter in terms of welded metal. The productivity of argon GTA is however limited by the diffusivity of the heat source. This aspect can be improved by changing the shielding gas composition introducing for instance helium or carbon dioxide to increase the arc heating power. Carbon dioxide has the economic advantage of its lower cost. A drawback is its corrosive effect on tungsten electrodes leading to arc instabilities when using more than a few percent CO₂. This drawback can be circumvented using a double-gas-shielded system, with inner flow of inert gas (usually argon) to protect the tungsten electrode and an external shielding flow of active gas with high heating power (such as CO₂). This method was investigated experimentally by Tanaka *et al.* (2006) and Lu *et al.* (2010). Their experimental investigations did show that CO₂ leads to a significant increase of the arc heating power compared to argon GTA. However experimental investigations do not allow measuring all the relevant properties needed to study and improve arc welding production processes. For instance, they do not provide the qualitative influence of composition on the arc pressure, and they do not allow doing the distinction between the different forms of heat transfer to the base metal. Modeling is used here to supplement experiments and reach a deeper insight into the influence of the composition of the shielding gas on the pressure force and the heat fluxes to a workpiece. The thermal plasma simulation model is described in section 2. The numerical setup and simulation results are presented in section 3.1 and 3.2, respectively. Finally the conclusion is in section 4.

2. MODEL

The magneto hydrodynamic model applies to the core of the electric arc (also called plasma core). The thermal fluid part of the model can be derived from a system of Boltzmann transport equations using kinetic theory, see (Choquet and Lucquin-Desreux, 2011). The plasma core is a Newtonian and thermally expansible fluid in local thermal equilibrium. In this study steady-state and laminar flow are also assumed. The electromagnetic part of the model is derived from the system of Maxwell equations, see (Choquet *et al.* 2012). Local electro-neutrality is verified since the Debye length is much smaller than the characteristic length of the welding arc, and the diffusion and thermo-diffusion currents due to electrons are small compared to the drift current. The characteristic time and length of the welding arc allow neglecting the displacement current compared to the current density, resulting in quasi-steady electromagnetic phenomena. The Larmor frequency is much smaller than the average collision frequency of electrons, implying a negligible Hall current compared to the drift current. Finally, the magnetic Reynolds number is much smaller than unity, leading to a negligible induction current compared to the drift current.

The system of equations governing the plasma core includes three fluid equations, namely the continuity equation, the Navier-Stokes equation and the enthalpy conservation equation, supplemented with two electromagnetic equations governing the electric potential V and the magnetic potential \vec{A} . The Lorentz gauge is used to uniquely define \vec{A} and V . This system of coupled equations can be written as

$$\nabla \cdot [\rho(T)\vec{u}] = 0 \quad (1)$$

$$\nabla \cdot [\rho(T)\vec{u} \otimes \vec{u}] - \vec{u} \nabla \cdot [\rho(T)\vec{u}] - \nabla \cdot \boldsymbol{\tau} = -\nabla P + \vec{J} \times \vec{B} \quad (2)$$

$$\nabla \cdot [\rho(T)\vec{u}h] - h \nabla \cdot [\rho(T)\vec{u}] - \nabla \cdot [\alpha(T)\nabla h] = \nabla \cdot (\vec{u}P) - P \nabla \cdot \vec{u} + \vec{J} \cdot \vec{E} - Q_{rad} + \nabla \cdot \left[\frac{5k_B\vec{J}}{2eC_p(T)} h \right] \quad (3)$$

$$\nabla \cdot [\sigma(T)\nabla V] = 0 \quad (4)$$

$$\Delta \vec{A} = \mu_o \sigma(T) \nabla V \quad (5)$$

It is supplemented with the following closure relations:

$$\boldsymbol{\tau}(\vec{u}, T) = \mu(T) (\nabla \vec{u} + (\nabla \vec{u})^T) - \frac{2}{3} \mu(T) (\nabla \cdot \vec{u}) \mathbf{I} \quad (6)$$

$$C_p(T) = \left(\frac{dh}{dT} \right)_P \quad (7)$$

$$\vec{E} = -\nabla V \quad (8)$$

$$\vec{J} = \sigma(T) \vec{E} \quad (9)$$

$$\vec{B} = \nabla \times \vec{A} \quad (10)$$

The thermal fluid variables are the fluid velocity \vec{u} , the pressure P , and the specific enthalpy h . Temperature $T = T(h)$ and density $\rho(T)$ are derived variables. $\boldsymbol{\tau}$ denotes the viscous stress tensor. In addition to density the temperature dependent thermal fluid properties are the radiation heat loss Q_{rad} , the thermal diffusivity $\alpha(T)$, the viscosity $\mu(T)$, and the specific heat at constant pressure $C_p(T)$. The derived electromagnetic variables are the electric field \vec{E} , the current density due to electron drift \vec{J} , and the magnetic flux density \vec{B} (also called magnetic field). $\sigma(T)$ denotes the temperature dependent electric conductivity. Finally \mathbf{I} is the identity tensor, k_B the Boltzmann constant, and e the elementary charge.

The fluid and electromagnetic parts of the model are tightly coupled. The last term on the right hand side of the Navier-Stokes equation (2) is the Lorentz force resulting from the induced magnetic field. This force, also called magnetic pinch force, is the main cause of plasma flow acceleration. The third term on the right hand side of the enthalpy conservation equation (3) is the Joule heating, and the last term a heat source due to the transport of electron enthalpy. The Joule heating is the largest heat source governing the plasma energy (and thus temperature). Besides the equations (4)-(5) governing electromagnetism are temperature dependent through the electric conductivity.

The radiation heat loss was tabulated using the net emission coefficients of Delalonde (1990). The thermodynamic

and transport properties were linearly interpolated from tabulated data implemented on a temperature range from 200 to 30 000 K, with a temperature increment of 100 K. For pure argon and pure carbon dioxide the data tables result from derivations done by Rat *et al.* (2001) and André *et al.* (2010) using kinetic theory. For the argon plasma with respectively 1% and 10% in mole of carbon dioxide the data tables were prepared doing an additional calculation step, based on the data for pure argon, pure carbon dioxide, and standard mixing laws. The mixing laws for calculating the specific heat and the enthalpy of a mixture use mass concentration as weighting factor, see (Sonntag *et al.* 2003). When applied to the calculation of the viscosity, the thermal conductivity and the electric conductivity of a mixture, the molar concentration is instead used as weighting factor, see (Kee *et al.* 2003).

The composition (in terms of species number densities) of an argon plasma and a carbon dioxide plasma at thermal equilibrium and atmospheric pressure is shown in Fig. 1. The specific heats of these two plasmas can be compared in Fig. 2 (left). The peaks observed at about 3 kK and 7.5 kK for the specific heat of the carbon dioxide plasma are related to dissociation reactions, see Fig. 1 (right). All the other peaks observed for both argon and carbon dioxide are associated with ionization reactions. The specific heat is much larger for the carbon dioxide plasma than for the argon plasma. At low temperature (below 1.5 kK) this difference is very significant: it reaches several orders of magnitude. The electric conductivities of these two plasmas can be compared in Fig. 2 (right). At low temperature the differences are quite small. From 2 kK they become much more pronounced. In the vicinity of 2.5 kK the electric conductivity of the carbon dioxide plasma is much larger (about 20%) than for the argon plasma.

The model was implemented in the open source simulation software OpenFOAM (www.openfoam.com). OpenFOAM was distributed as OpenSource in 2004. This simulation software is a C++ library of object-oriented classes that can be used for implementing solvers for continuum mechanics. Due to the availability of the source code, its libraries can be used to implement new solvers for other applications. The current implementation is based on the buoyantSimpleFoam solver of OpenFOAM-2.1.x, which is a steady-state solver for buoyant, turbulent flow of compressible fluids. The partial differential equations of this solver are discretized using the finite volume method.

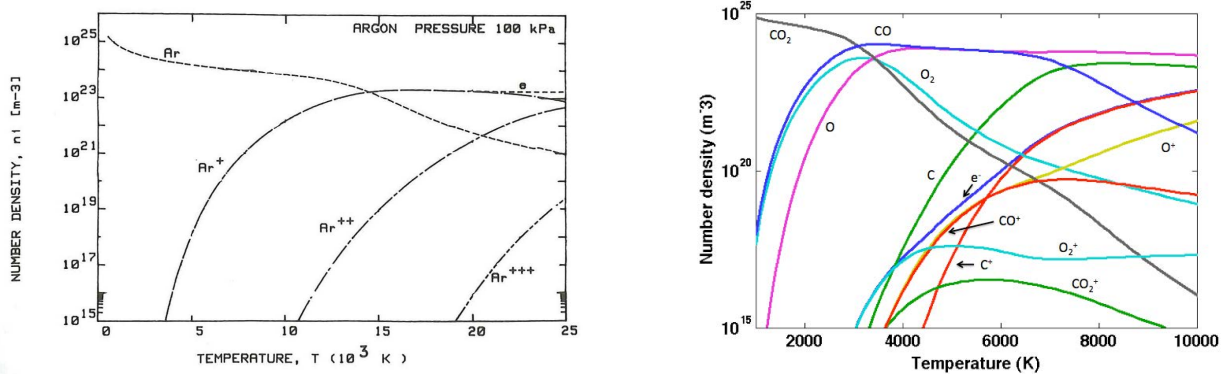


Fig. 1. Temperature dependence of the equilibrium composition (species number densities) of a plasma at atmospheric pressure. Left: argon plasma, see (Boulos *et al.* 1994); Right: carbon dioxide plasma, see (Colombo *et al.* 2011).

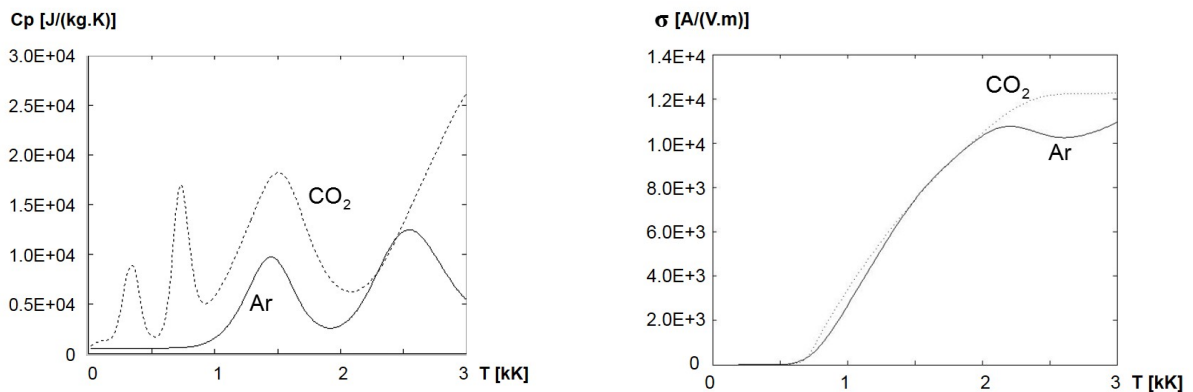


Fig. 2. Left: Specific heat as a function of temperature; Right: Electric conductivity as function of temperature. Solid line: argon plasma at atmospheric pressure; dotted line: carbon dioxide plasma at atmospheric pressure.

3. APPLICATION TO AN ELECTRIC ARC

A 200 A and 2 mm short GTA was simulated to investigate the influence of the composition of the shielding gas mixture on the arc pressure force and the heat fluxes on the workpiece. Four different shielding gas mixtures were analyzed: pure argon, argon mixed with respectively 1% and 10% in mole of carbon dioxide, and pure carbon dioxide. In the two latter cases the inner gas flow that needs to be used to protect the tungsten electrode was not included in the simulations.

3.1 Numerical setup

The configuration is sketched in Fig. 3. The electrode, of radius 1.6 mm, has a conical tip of angle 60° truncated at a tip radius of 0.5 mm. The electrode is mounted inside a ceramic nozzle of internal and external radius 5 mm and 8.2 mm, respectively. The shielding gas enters the nozzle at room temperature and at an average mass flow rate of $1.66 \times 10^{-4} \text{ m}^3/\text{s}$.

Electrode and base metal were modelled through boundary conditions. In other words the interior of the electrode and base metal were not included in the calculation domain. Only few published experimental measurements do provide the data needed for setting the boundary conditions on the electrode surface and the base metal surface. The experimental study of Haddad and Farmer (1985) was used to set the boundary conditions summarized in Table 1.

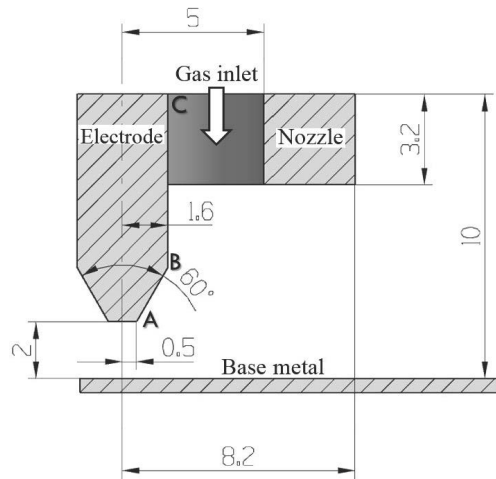


Fig. 3. Schematic representation of the test case.

Table 1. Boundary conditions

	Cathode ^(a)			Anode	Nozzle	Inlet	Outlet
	Tip	AB	BC				
\vec{u}	$\vec{u} \cdot \vec{n} = 0$	$\vec{u} \cdot \vec{n} = 0$	$\vec{u} \cdot \vec{n} = 0$	$\vec{u} \cdot \vec{n} = 0$	$\vec{u} \cdot \vec{n} = 0$	parabolic	$\partial_{\vec{n}} \vec{u} = 0$
h or T	20000K	linear ^(b)	linear ^(b)	linear ^(c)	$\partial_{\vec{n}} h = 0$	300K	$\partial_{\vec{n}} h = 0$
V or \vec{J}	$J_0 \vec{n}$	$J_{AB} \vec{n}^{(d)}$	$\vec{J} \cdot \vec{n} = 0$	$V = 0$	$\partial_{\vec{n}} V = 0$	$\partial_{\vec{n}} V = 0$	$\partial_{\vec{n}} V = 0$
\vec{A}	$\partial_{\vec{n}} \vec{A} = 0$	$\partial_{\vec{n}} \vec{A} = 0$	$\partial_{\vec{n}} \vec{A} = 0$	$\partial_{\vec{n}} \vec{A} = 0$	$\partial_{\vec{n}} \vec{A} = 0$	$\partial_{\vec{n}} \vec{A} = 0$	$\vec{A} \cdot \vec{n} = 0$

\vec{n} denotes the local unit vector normal to the boundary.

^(a) see Fig. 3 for the location of the points A, B, and C.

^(b) with T = 20000K in A, 3200K in B, and 2700K in C.

^(c) with T = 14000K below the tip and 7000K at 5 mm from the symmetry axis.

^(d) see (12).

The constant J_0 satisfies

$$I = \int_0^{r_0} 2\pi r J_0 dr + \int_0^{L_0} 2\pi r J_{AB}(\eta) d\eta \quad (11)$$

where I is the imposed current, r denotes the distance to the symmetry axis on the electrode tip, and η is the distance to point A along the cathode tip bevel AB . $L_0 = 1\text{mm}$ delimits the extension of the conducting cathode spot of radius $r_h = r_0 + L_0 \sin 30$.

The current density on the cathode boundary AB (see Fig. 3) is normal to AB and set to

$$\begin{aligned} J_{AB}(\eta) &= J_0 \left(1 - \frac{\eta}{L_0}\right) \quad \text{if } \eta < L_0 \\ J_{AB}(\eta) &= 0 \quad \text{if } \eta \geq L_0 \end{aligned} \quad (12)$$

The calculations were done using 25 uniform cells along the 0.5 mm tip radius, 100 uniform cells between the electrode and the base metal along the symmetry axis, and a total number of 136250 cells. A mesh sensitivity study has been done concluding that the present mesh is sufficiently fine.

3.2 Simulation results

Results obtained for the pure argon shielding gas and the pure carbon dioxide shielding gas are first compared. The calculated temperature contours in a radial section zoomed between the electrode tip and the base metal are plotted in Fig. 4 (left). The left section of the figure was obtained with the carbon-dioxide plasma while the right section was obtained with the argon plasma. Comparing these T-contours it can be seen that the carbon-dioxide plasma is more constricted than the argon plasma (see the outer contour corresponding to 12 kK). This thermal constriction is due to the larger specific heat (especially at low temperature) of the CO_2 plasma compared to the Ar plasma.

The calculated current density contours in the same region are plotted in Fig. 4 (right). As previously the left section of the figure was obtained with the carbon-dioxide plasma while the right section was obtained with the argon plasma. The zone with high electrical conduction which is located below the electrode tip is broader for the carbon-dioxide plasma than for the argon plasma (see the inner contour reaching the base metal; $J=10\text{MA/m}^2$). This is due to the larger electric conductivity of the CO_2 plasma compared to the Ar plasma at the large temperatures ($T \geq 20$ kK) observed in a close vicinity below the electrode tip (see Fig. 5 (left)).

Results obtained with the four different compositions of the shielding gas are now compared. The calculated temperature is plotted along the symmetry axis in Fig. 5 (left), and along the radial direction 1 mm above the anode in Fig. 5 (right). It can be seen that the presence of carbon dioxide results in an increased arc temperature (Fig. 5), and a constriction of the temperature field above the base metal (Fig. 5 (right)). With 10% CO_2 (resp. 100%) the maximum arc temperature is about 250 K (resp. about 2000 K) larger than with argon alone. The thermal constriction is not observed with 1% CO_2 but it is already very significant when using 10% CO_2 . It results from the specific heat which is several orders of magnitude larger for CO_2 than for Ar at temperature below 1 kK (see Fig. 2 (left)).

The calculated velocity is plotted along the symmetry axis in Fig. 6 (left), and along the radial direction 1 mm above the anode in Fig. 6 (right). The maximum velocity (on the symmetry axis) increases from about 200 m/s for pure argon to about 325 m/s for pure carbon dioxide. This increase in maximum velocity when increasing the CO_2 concentration is due to an increased Lorentz force, itself resulting from the constriction of the current density lines observed on the cathode tip in Fig. 4 (right). The concentration in CO_2 has almost no influence on the extent of the plasma above the base metal, see Fig. 6 (right). It can also be seen in Fig. 7 that the large increase in plasma jet velocity observed when increasing the CO_2 concentration is not associated with an increase of the arc pressure on the base metal, see Fig. 7. On the contrary the arc pressure decreases when increasing the CO_2 concentration in the shielding gas. This is due to the temperature dependence of the plasma density: at high temperature the Ar plasma density becomes significantly larger than the CO_2 plasma density.

The heat flux Q_J due to the current density is plotted in Fig. 8 (left). The maximum value of Q_J is observed to increase by 1.5%, 34% and more than 150% when increasing the CO_2 concentration to 1%, 10% and 100%, respectively. The heat flux Q_T due to the temperature gradient is plotted in Fig. 8 (right). The slope discontinuity observed in $y = 0.5$ mm for Q_T results from the temperature assumed on the base metal boundary. The maximum value of Q_T is observed to increase by almost 1%, 13% and more than 47% when increasing the CO_2 concentration to 1%, 10% and 100%, respectively. In addition, the heat flux Q_T to the base metal is a little more constricted when increasing the CO_2 concentration.



Fig. 4. Zoom of contours between electrode and base metal. Left: temperature T and Right: current density J (with CO_2 in each left section, Ar in right section). From large to small radius the T -contours (resp. J -contours) correspond to 12, 14, 16, 18, 20, 22 and 24 kK (resp. 1, 2.5, 5, 7.5, 10, 25, and 50 MA/m^2).

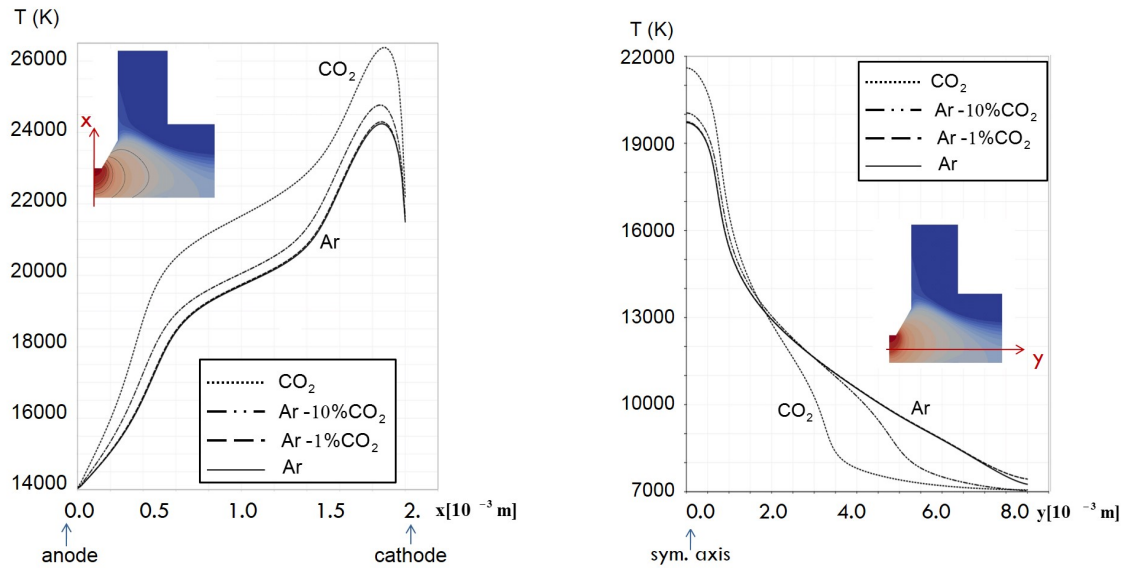


Fig. 5. Temperature. Left: along the symmetry axis; Right: along the radial direction, 1 mm above the anode.

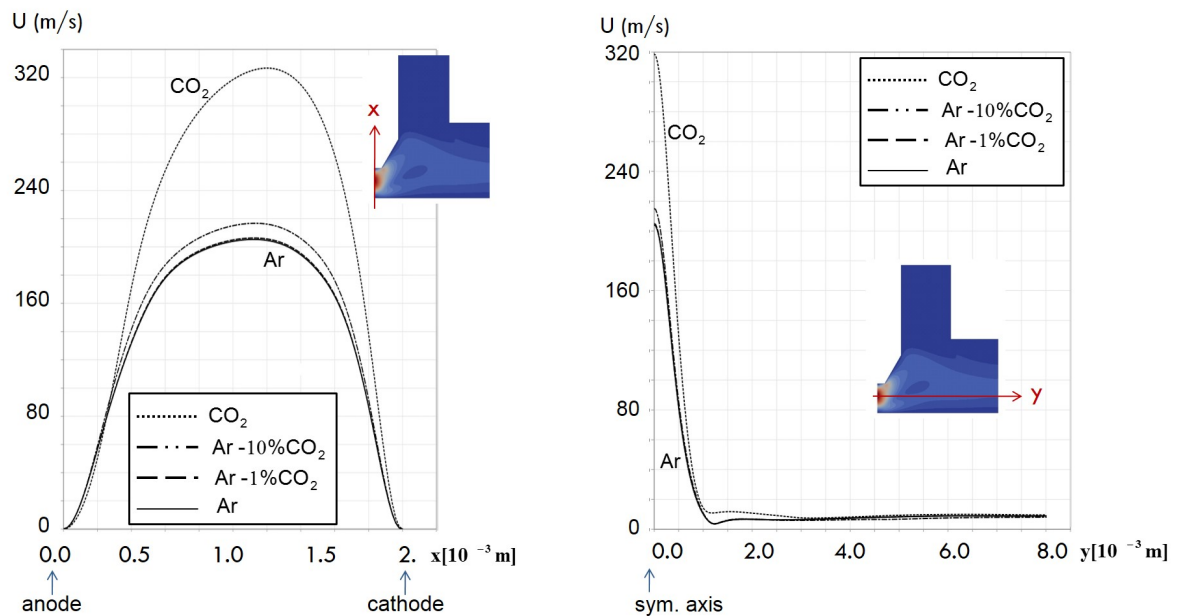


Fig. 6. Velocity. Left: along the symmetry axis. Right: along the radial direction, 1 mm above the anode.

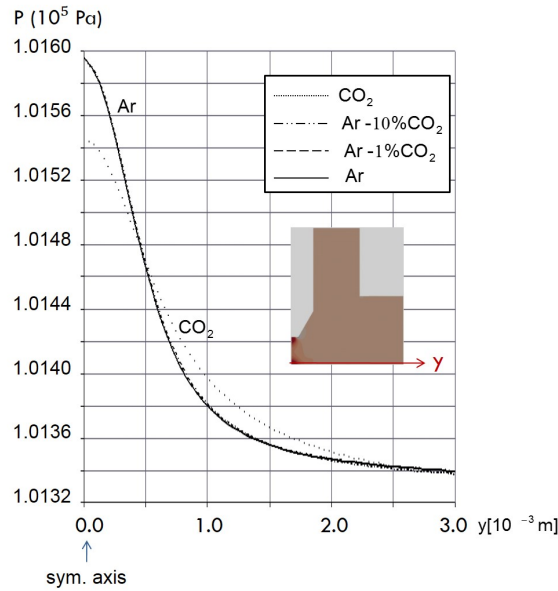


Fig. 7. Pressure on the base metal along the radial direction

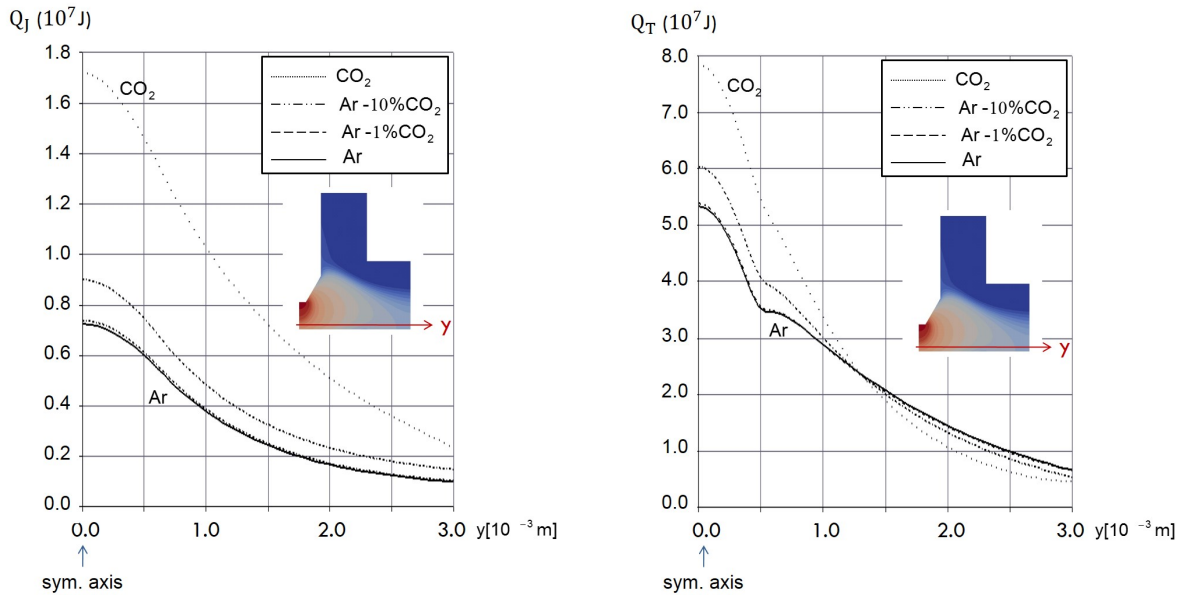


Fig. 8. Heat flux to base metal (along the radial direction).
Left: due to temperature gradients; Right: due to electron enthalpy.

4. CONCLUSION

This study focused on the modeling and simulation of an electric arc heat source, coupling thermal fluid mechanics with electromagnetics. The model was implemented in the open source software OpenFOAM. It was applied to evaluate the influence of the amount of CO₂ in an argon shielding gas on plasma arc properties. The simulation results show a thermal constriction of the arc and an increase in heat flux to the base metal when increasing the molar fraction of carbon dioxide. These results are in agreement with the experimental observations of Tanaka *et al.* (2006).

The simulation model provides also other relevant information that experimental investigations do not yet allow measuring. They show that the arc jet velocity is significantly increased while the pressure on the base metal is on the contrary reduced when increasing the molar fraction of carbon dioxide. It also shows that the heat flux due to the current density and due to the temperature gradient do not increase in the same proportions when increasing the molar fraction of carbon dioxide. In addition the former does not seem to be constricted while the latter is constricted.

These results are qualitative results since the boundary conditions on the electrode and the base metal were imposed using available experimental data. To further enhance the predictive capability of the simulation model and allow a quantitative comparison, the temperature and current density distributions on the electrode surface should be calculated rather than set. In that aim the system of equations describing the arc should be extended to include the electrode and the base metal. This requires coupling properly these different regions and modeling the so-called electrode sheaths, as further detailed by Javidi *et al.* (2014).

ACKNOWLEDGMENT

This work was supported by KK-foundation in collaboration with ESAB. Håkan Nilsson was in this work financed by the Sustainable Production Initiative and the Production Area of Advance at Chalmers. These supports are gratefully acknowledged.

REFERENCES

- André, P., J. Aubreton, S. Clain, M. Dudeck, E. Duffour, M. F. Elchinger, B. Izrar, D. Rochette, R. Touzani, and D. Vacher (2010). Transport coefficients in thermal plasma. Applications to Mars and Titan atmospheres. *European Physical Journal D*, **57**, pp. 227-234.
- Boulos, M.I., P. Fauchais P. and E. Pfender (1994). *Thermal Plasmas, Fundamentals and Applications, Vol. 1*. Plenum Press, New York.
- Choquet, I. and B. Lucquin-Desreux (2011). Non equilibrium ionization in magnetized two-temperature thermal plasma. *Kinetic and Related Models*, **4**, pp. 669-700.
- Choquet, I., A. Javidi Shirvan, and H. Nilsson (2012). On the choice of electromagnetic model for short high-intensity arcs, applied to welding. *Journal of Physics D: Applied Physics*, **45**, 205203 (14pp).
- Colombo, V., E. Ghedini and P. Sanibondi (2011) Two-temperature thermodynamic and transport properties of carbon-oxygen plasmas *Journal of Physics D: Applied Physics*, **20**, 035003 (8pp).
- Delalondre C (1990). *Modélisation aérothermodynamique d'arcs électriques à forte intensité avec prise en compte du déséquilibre thermodynamique local et du transfert thermique à la cathode*. PhD Thesis Rouen University, France.
- Haddad, G.N. and A.J.D. Farmer (1985). Temperature measurements in gas tungsten arcs. *Welding Journal* **24**, pp. 339-342.
- Javidi Shirvan, A., I. Choquet, H. Nilsson (2014). Modelling of electrode-arc coupling in electric arc welding, Swedish Production Symposium SPS14, submitted.
- Kee, R. J., M. E. Coltrin, P. Glaborg (2003). *Chemically reacting flow. Theory and Practice*, Wiley Interscience.
- Lu, S., H. Fujii, and K. Nogi (2010). Weld shape variation and electrode oxidation behavior under Ar-(Ar-CO₂) double shielded GTA welding. *Journal of Material Science and Technology*, **26**, pp. 170-176.
- Rat, V., A. Pascal, J. Aubreton, M.F. Elchinger, P. Fauchais and A. Lefort (2001). Transport properties in a two-temperature plasma: theory and application. *Physical Review E*, **64**, 026409 (20pp).
- Sonntag, R.E., C. Borgnakke, and G.J. Van Wylen (2003). *Fundamentals of thermodynamics*, Wiley, 6th edition.
- Tanaka, M., S. Tashiro, M. Ushio, T. Mitab, A. B. Murphy, J. J. Lowke (2006). CO₂-shielded arc as a high-intensity heat source. *Vacuum* **80**, pp. 1195-1198.